www.nature.com/scientificreports

scientific reports

Check for updates

OPEN

Enhanced electrochemical detection of dopamine and uric acid using Au@Ni-MOF and employing 2D structure DFT simulation

Feng Zhou[1], Limei Gai[2]✉, Hua Liu[1], Danfeng Qin[3], Tushagu Abudouwufu[4] & Yi Liu[5]✉

The accurate and expeditious detection of minute biomolecules within human body fluids holds paramount significance in the advancement of novel electrode materials. In this research, a novel non-enzyme electrochemical sensor was constructed. It was founded on Au@Ni-MOF ($Ni(CH_3CO_2)_2$) hybrids, with Ni(II) (nickel acetate) serving as the precursor. Specifically, $[Ni_3(BTC)_2]_n$ (H_3BTC = 1,3,5-trimesic acid) featuring coordinatively unsaturated Ni(II) sites and decorated with gold nanoparticles was synthesized via an in-situ growth methodology. The Au@Ni-MOF hybrids exhibit outstanding electrochemical and electrocatalytic characteristics, attributable to the meticulous assembly of AuNPs and Ni-MOF. The Au@Ni-MOF ($Ni(CH_3CO_2)_2$)/SPCE was fabricated onto the surface of the screen-printed electrode (SPCE). Subsequently, its electrochemical performance was probed for the discrete and concurrent quantification of dopamine (DA) and uric acid (UA) in 0.01 M phosphate-buffered saline through differential pulse voltammetry (DPV) and electrochemical impedance spectroscopy (EIS). Notably, the cathodic peak current manifested a linear correlation with the DA and UA concentrations across an extensive range, spanning from 0.1 μM to 2 mM for DA and from 0.5 μM to 1.5 mM for UA, respectively. This sensor is applicable in non-enzyme sensing of DA and UA. Additionally, the adsorption energy and bond length of the 2D structures of Ni-MOF and Au@Ni-MOF ($Ni(CH_3CO_2)_2$) were ascertained via DFT simulations, thereby affording valuable insights into the interaction mechanisms between biomolecules and the surfaces of these 2D structures.

Keywords Au@Ni-MOF ($Ni(CH_3CO_2)_2$), Dopamine, Uric acid, Electrochemical sensor, DFT simulation

Crucial small biomolecules, namely dopamine (DA) and uric acid (UA), play essential roles in life processes and are integral to human metabolism[1]. These molecules are commonly found together in the extracellular fluid of the central nervous system and serum, where they hold significant physiological importance[1–3]. Among these small biomolecules, DA is an important neurotransmitter substance that controls the central nervous system, and cardiovascular, renal, and hormonal functions, which is also greatly relevant to addiction to smoking or drugs and in Parkinson's disease[4–6]. UA is an end product of purine metabolism, and it is excreted from human biological fluids via urine, feces, and sweat[7,8]. However, the changes in the concentration of UA in the above-mentioned fluids can cause various diseases and disorders, such as gouty nephropathy, gout arthritis, anemia, and hyperuricemia[9,10]. Hence, it is very important to rapidly develop a good method for the individual and simultaneous determination of DA and UA in the fields of nerve physiology, making diagnoses, and controlling medicine.

In the past few decades, the studies and employment of nanoparticles have attracted tremendous attention from more and more researchers[11]. Among them, metal-organic framework (MOF) particles as crystalline

[1]School of Engineering, Guangzhou College of Technology and Business, Guangzhou 510880, Guangdong, People's Republic of China. [2]National-Local Joint Engineering Research Center of Harbor Oil & Gas Storage and Transportation Technology, Zhejiang Key Laboratory of Pollution Control for Port- Petrochemical Industry, School of Petrochemical Engineering & Environment, Zhejiang Ocean University, Zhoushan 316022, People's Republic of China. [3]School of Medicine, Guangxi University of Science and Technology, Liuzhou 545006, Guangxi, People's Republic of China. [4]School of Pharmacy and Food Science, Zhuhai College of Science and Technology, No. 8 Anji East Road, Jinwan District, Zhuhai 519041, People's Republic of China. [5]State Key Laboratory of Functional Materials and Devices for Special Environments Conditions, Xinjiang Key Laboratory of Electronic Information Materials & Devices, Xinjiang Technical Institute of Physics & Chemistry of CAS, 40-1 South Beijing Road, Urumqi 830011, People's Republic of China. ✉email: gailimei@zjou.edu.cn; liu_yi@ms.xjb.ac.cn

hybrid materials are the most popular candidates, which are made up of metal ions and organic ligands to form some different 3D structures[12,13]. For example, 1,3,5-benzene tricarboxylic acid is commonly known as trimesic acid (H_3BTC), which is a tridentate ligand that can form different MOFs with different metal salt in the same synthetic procedures[7]. To stimulate more advanced application potential and value of MOF in particle state, a great diversity of MOF hybrids has been synthesized by changing the metal or organic sources, synthetic conditions, and post-synthetic modification, which are widely used in energy storage devices, catalysts, separation, ion conduction, molecular recognition, gas storage, sensing, drug delivery, and others[11,14,15]. Especially, some researchers highlight MOF-based electrochemical sensors for sensitive and selective detection of DA and UA in our body fluids due to the advantage of large internal surface area, tunable porosity, structural, and functional diversity, and unsaturated metallic sites[14–16]. In addition, Nickel-based MOFs have been widely used in different fields due to their low cost and natural abundance[14,17]. However, MOFs also had some obvious disadvantages, such as poor conductivity, bad adhesion, irregular shape, and easier to aggregate[11,15]. Therefore, it is still a huge challenge to obtain pure MOFs as electrochemical electrodes with excellent high sensitivity and extraordinary catalytic properties for the detection of small biomolecules. To solve these drawbacks, some scientists are focused on the sensors by using MOF hybrids with nano-sized precious metal nanoparticles (NPs), such as Pt, Au, Ag, and so on[18,19]. Among the more extensively exploited precious metal nanoparticles (NPs), gold nanoparticles (AuNPs) have attracted much more special attention as chemical modifiers decorated MOFs due to their excellent specific surface area, small pore size, high electrical conductivity, high catalytic activity, and catalytic selectivity[20–23].

In addition, Density Functional Theory (DFT) simulation is a powerful tool for understanding the electronic structure and properties of materials at the atomic level[24,25]. DFT simulations can be employed to investigate the interaction between the Au@Ni-MOF ($Ni(CH_3CO_2)_2$) and DA/UA molecules, providing valuable insights into the underlying mechanisms of the electrochemical detection process.

In this work, one novel one-dimensional nickel (II) with 1,3,5-benzene tricarboxylic acid formed the Ni-MOF ($Ni(CH_3CO_2)_2$) with the precursors of Ni (II), and then using gold nanoparticles (AuNPs) decorated the Ni-MOF ($Ni(CH_3CO_2)_2$) composites modified screen-printed electrode were fabricated via a solvothermal method by using ultrasonic treatment to get Au@Ni-MOF ($Ni(CH_3CO_2)_2$) hybrids for the individual and simultaneous electrochemical detection of DA and UA. We demonstrated that the current approach can not only obtain the regular shape of Ni-MOFs ($Ni(CH_3CO_2)_2$) with large surface areas but also attach all gold nanoparticles on the surface of the complex three-dimensional (3D) frameworks: MOF layer to improve the conductivity and enhanced electrocatalytic performance of Au@Ni-MOF ($Ni(CH_3CO_2)_2$). Moreover, compared with Au@Ni-MOF ($Ni(CH_3CO_2)_2$), the as-prepared Au@Ni-MOF ($Ni(CH_3CO_2)_2$) exhibited better broad linearity, higher sensitivity, lower LOD (limit of detection), better selectivity, reproducibility, and long-term stability for the detection of DA and UA due to its large specific surface areas, large pore diameter, regular structure, as well as a higher content of AuNPs. Therefore, Au@Ni-MOF ($Ni(CH_3CO_2)_2$) provides an efficient and fast candidate material for electrochemical sensors. By integrating experimental data with DFT simulations, a comprehensive understanding of the interactions between the nanomaterial and target analytes will be achieved, enabling the development of highly sensitive and selective electrochemical sensors for practical applications in healthcare, environmental monitoring, and beyond. This work contributes to the advancement of materials science and sensor technology, offering innovative solutions for the accurate and efficient detection of neurochemicals and biomarkers. Notably, the Ni-MOF material holds great promise in providing cost-effective and sustainable alternatives in the field of medical diagnostics, where it can potentially replace expensive and less environmentally friendly sensing materials, thereby facilitating more accessible and greener healthcare solutions.

Experimental

Materials

Gold (III) chloride trihydrate ($HAuCl_4·3H_2O$), trisodium citrate ($Na_3C_6H_5O_7$), dopamine (DA), and uric acid (UA) were purchased from Aldrich, USA. Ethanol ($CH_3CH_2OH_2$, 95%), *N*,*N*-dimethylformamide (DMF), Nafion, potassium chloride (KCl), potassium ferricyanide ($K_3[Fe(CN)_6]$), and potassium ferricyanide ($K_4[Fe(CN)_6]·3H_2O$) were purchased from Systerm, Malaysia. Phosphate buffer solution (PBS) was prepared with a standard stock solution of sodium dihydrogen phosphate monohydrate ($NaH_2PO_4·H_2O$, 99%) and disodium hydrogen phosphate dihydrate ($Na_2HPO_4·2H_2O$, 99.5%) and adjusted pH value with phosphoric acid (H_3PO_4) and sodium hydroxide (NaOH) which were purchased from Merck, Germany. Nickel (II) acetate tetrahydrate ($Ni(CH_3CO_2)_2·4H_2O$), and 1,3,5-trimesic acid (H_3BTC) were of analytical grade and were purchased from Systerm, Malaysia. Screen-printed electrodes (SPCEs) were purchased from DS Dropsens, Spain. Samples of human serum were bought from Aldrich, China. Human urine was taken from a 5-year-old baby. Deionized water was used in all the experiments. Unless otherwise specified, all the materials and reagents were used as received without conducting any purification process.

Preparation of AuNPs

Preparation of AuNPs via an in-situ method that uses a water bath instead of reflux[7]. AuNPs were prepared by the citrate reduction of $HAuCl_4$. Curtly,100 mL of 1.0 mmol% $HAuCl_4$ was poured into a 250 mL round-bottomed flask. The mixture was heated in a water bath until boiling. With constant stirring, trisodium citrate solution (1.0% w/v in 4.0 mL) was drop-wisely added. The color of the solution changed from pale yellow to black and finally to a red wine color within a few minutes, and then the reaction was carried out for 1 h. After the final solution was cooled down, the washing process was carried out by centrifugation. Finally, the product was stored in the refrigerator.

Preparation of Au@Ni-MOF (Ni $(CH_3CO_2)_2$) hybrids

3 mmol Ni $(CH_3CO_2)_2 \cdot 4H_2O$ and 2 mmol H_3BTC were dissolved in DMF (90 mL) and deionized water (10 ml) mixture with the help of ultrasonication. The blended solution was transferred into a conical flask and stirred for 5 min at room temperature. Afterward, the glass bottle was transferred into a bath sonicator and held for 1 h. Then, the bright green mixture was 3 times washed by DMF to remove extra Ni(II), and then collected by centrifugation at 9900 rpm for 15 min, furnishing the bright green product as a residue, which was several times washed with chloroform and centrifuged to remove DMF. The product was dried using an oven at 90 °C for 4 h. Afterward, the Ni-MOF (Nickel acetate) powder was mixed with AuNPs solution 36 mL (1 mM) in ethanol and further stirred for 1 h at room temperature, followed by transfer to the oven. Finally, the green product was dried using an oven at 90 °C for 6 h for further characterization. The obtained samples were prepared with different volumes of AuNPs solutions labeled as Au@Ni-MOF ($Ni(CH_3CO_2)_2$) (2.0 mL), Au@Ni-MOF ($Ni(CH_3CO_2)_2$) (12.0 mL), and Au@Ni-MOF ($Ni(CH_3CO_2)_2$) (36.0 mL), respectively.

Fabrication of Au@Ni-MOF ($Ni(CH_3CO_2)_2$) hybrids modified SPCE

It is very highly desirable to develop a highly sensitive and facile sensing platform for DA and UA. Therefore, Au@Ni-MOF ($Ni(CH_3CO_2)_2$)/SPCE-modified electrodes were both prepared by a one-step in-situ method using nickel acetate salt as the metal precursor, as shown in Fig. 1. Firstly, 1.5 mg Au@Ni-MOF ($Ni(CH_3CO_2)_2$) composites were added to 1.5 mL of ethanol to form solution. Subsequently, this solution was completely dispersed using ultrasonication to require a homogeneous solution. Then, for the fabrication of the Au@Ni-MOF ($Ni(CH_3CO_2)_2$), 50 µL solution was dispersed and then ultrasonicated for 30 min to obtain a uniform suspension: suspension. The SPCE electrode surface was washed in de-ionized water and dried in an N_2 atmosphere before being used. Next, the suspension (5.0 µL) was dropped on the surface of the well-washed SPE and cast with Nafion (wt. 5.0%, 2.0 µL), and dried under ambient conditions, repeated this operation 5 times.

Characterization

The morphology of the samples was examined by using a scanning electron microscope (SEM) (Zeiss Supra 55 VP, Germany) equipped with an energy-dispersive X-ray (EDX) (BRUKER X-FLASH-SDD-5010, Germany) accessory. High-resolution transmission electron microscopy (HR-TEM) (Hitachi, HT-7700, Tokyo, Japan) was used to characterize the shape and particle size analyses of AuNPs. The measurement of particle size of all the materials was obtained via an Image J Version 1.53t 24 August 2022 (USA). X-ray photoemission spectroscopy (XPS) was performed with a VGS ESCALAB 210 instrument using monochromatic Mg K X-radiation, which was operated in the constant-pass energy mode. The working pressure in the analysis chamber was typically 5×10^{-10} Torr. Data analysis was performed by a fitting program using properly mixed Lorentzian–Gaussian functions after background subtraction according to the Shirley method. Surface atomic compositions were determined using standard XPS cross-sections. The specific surface area was confirmed by the Brunauer-Emmett-Teller (BET) method. The crystalline phase and structure of the Au@Ni-MOF ($Ni(CH_3CO_2)_2$) composite was analyzed by using a Philips X'pert system X-ray powder diffractometer with Cu Kα radiation (λ = 1.5418 Å) in the 2θ range of 4–80. All the pH measurements were recorded by using a pH meter (Metrohm, model 827).

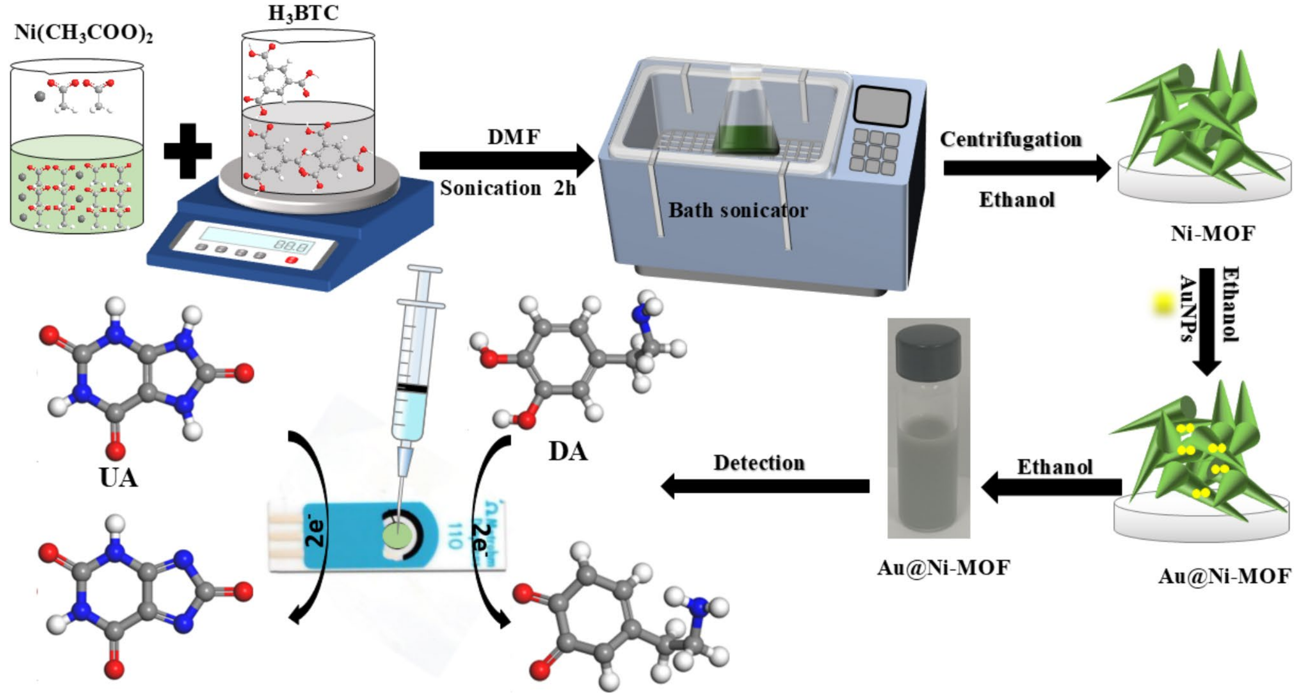

Fig. 1. Fabrication procedure of Au@Ni-MOF ($Ni(CH_3CO_2)_2$)/SPCE composite modified electrode.

Electrochemical experiments

The electrochemical experiments were conducted by dipping the Au@Ni-MOF ($Ni(CH_3CO_2)_2$)-modified SPCE in real water samples. The modified electrode was scanned in 0.01 M PBS (pH = 6.0), and then in PBS containing DA and UA with desired concentrations. Moreover, the detection of DA and UA was performed using linear sweep voltammetry in a negative-going scan of 0.2 to 0.6 V. Cyclic voltammetry (CV) and differential pulse voltammetry (DPV) were carried out using a potentiostat (Dropsense, mSTAT8000P) while another potentiostat (VrsaStat 3-300, Princeton, USA) was used for electrochemical impedance spectroscopy (EIS) studies. The electrochemical impedance spectroscopy (EIS) (0.1–100000 Hz) technique was carried out in 5 mmol·L^{-1} $[Fe(CN)_6]^{3-/4-}$ solution with an amplitude of 5 mV. All measurements were done at room temperature.

Computational method

DA, UA, two-dimensional Ni-MOF ($Ni(CH_3CO_2)_2$), and Au@Ni-MOF ($Ni(CH_3CO_2)_2$) structures were generated using ChemDraw software. The three-dimensional representations of DA and UA, along with the 2 × 2 × 2 supercell models of Ni-MOF ($Ni(CH_3CO_2)_2$) and Au@Ni-MOF ($Ni(CH_3CO_2)_2$) were constructed utilizing Materials Studio 6.1 software. Furthermore, electronic calculations for assessing the interactions between the target analytes and our materials were conducted through density functional theory (DFT), employing the general gradient approximation (GGA) within the Perdew-Burke-Ernzerhof (PBE) framework[26]. All calculations were done using a 2 × 2 × 2 k-point mesh and a cutoff energy of 500 eV.

Results and discussion

Characterization of the Au@Ni-MOF (Ni(CH3CO2)2) composites

High-resolution Transmission Electron Microscopy (HR-TEM) images were obtained for the gold nanoparticles (AuNPs) synthesized by reducing chloroauric acid with sodium citrate, as shown in Fig. 2A. The resulting AuNPs exhibited a polyhedral morphology. Furthermore, the AuNPs were monodispersed and relatively uniform, with an average physical diameter of 22.54 ± 5.897 nm measured across 30 particles (inset of Fig. 2A). These results indicate that we successfully synthesized monodispersed and sufficiently small AuNPs.

Figure 2B depicts SEM images of Ni-MOF ($Ni(CH_3CO_2)_2$), revealing a crystal lattice arranged in a layered structure, composed of identical building blocks typical of Metal-Organic Frameworks (MOFs). The morphology observed through SEM analysis shows a slender, needle-like 3D structure, highlighting the crystalline nature and layer-by-layer assembly characteristic of Ni-MOFs. According to previous investigations[7,27], certain Ni-based MOFs exhibit a spherical structure when synthesized using trimesic acid and nickel nitrate hexahydrate. This phenomenon suggests that employing the same organic ligands and metal ions but varying the clusters coordinated to the organic ligands, can result in the formation of MOF materials with different morphologies. In addition, Fig. 2C–E shows SEM images of Au@Ni-MOF ($Ni(CH_3CO_2)_2$), all of which exhibit the same morphologies as Ni-MOF ($Ni(CH_3CO_2)_2$). Specifically, Fig. 2D shows an enlarged view of the Au@Ni-MOF ($Ni(CH_3CO_2)_2$) structure, where it can be observed that small-sized AuNPs are deposited on the surface of the Au@Ni-MOF ($Ni(CH_3CO_2)_2$) composite.

The corresponding energy dispersive spectrometer (EDS) mapping results are presented in Fig. 2F,G, demonstrating that the elements oxygen (O), carbon (C), nickel (Ni), and gold (Au) are evenly distributed throughout the as-prepared material. This uniform distribution indicates a homogeneous composition of the Au@Ni-MOF ($Ni(CH_3CO_2)_2$) composite, ensuring consistent properties and performance across the material[11]. Furthermore, Fig. 2H presents the Energy Dispersive X-ray (EDX) spectrum, illustrating the elemental composition of the Au@Ni-MOF ($Ni(CH_3CO_2)_2$) composite. The accompanying table of weight percentages for the four elements, shown in Fig. 2I, reveals the presence of carbon (C) at 31.42%, oxygen (O) at 40.79%, nickel (Ni) at 26.77%, and gold (Au) at 0.69%. This analysis confirms the successful incorporation of a small amount of AuNPs on the surface of the Ni-MOF ($Ni(CH_3CO_2)_2$) composite.

X-ray powder diffraction (XRD) was further employed to investigate the structure of the Ni-MOF ($Ni(CH_3CO_2)_2$) and Au@Ni-MOF ($Ni(CH_3CO_2)_2$) composites. As shown in Fig. 3A, the XRD patterns of both Ni-based MOF powders exhibit sharp peaks consistent with previous reports[7,27]. Compared with pure Ni-MOF ($Ni(CH_3CO_2)_2$), the XRD peaks of Au@Ni-MOF ($Ni(CH_3CO_2)_2$) exhibit a similar pattern, with the notable addition of an extra peak at $2\theta = 38.2°$ corresponding to AuNPs[28]. This additional peak aligns well with the characteristic peaks of AuNPs observed in our analysis. These results confirm the successful formation of the Ni-based MOF structure. The specific surface area was determined using the single-point Brunauer-Emmett-Teller (BET) method, with results displayed in Fig. 3B and Table S1. Both Ni-MOF ($Ni(CH_3CO_2)_2$) and Au@Ni-MOF ($Ni(CH_3CO_2)_2$) samples exhibited type (IV) isotherms, indicative of a microporous structure consistent with prior literature[29]. The BET analysis revealed that the BET surface area of Au@Ni-MOF (10.0816 m²/g) was lower than that of Ni-MOF (12.7379 m^2/g), suggesting that the incorporation of AuNPs affected the overall surface area of the composite. Additionally, pore size distributions were calculated from nitrogen sorption data using the Barrett Joyner Halenda (BJH) method, as summarized in Table S1. The results indicate a reduction in porosity for the Au@Ni-MOF ($Ni(CH_3CO_2)_2$) composite compared to Ni-MOF ($Ni(CH_3CO_2)_2$), as evidenced by a smaller volume in the BJH desorption branch and a decrease in pore size. This reduction suggests that the presence of AuNPs alters the pore characteristics of the composite material.

The XPS survey spectrum presented in Fig. 4 serves to corroborate the elemental composition, specifically confirming the presence of carbon (C), oxygen (O), nickel (Ni), and gold (Au) constituents. In the C 1s region, as illustrated in Fig. 4A, the observed peak at 285.2 eV aligns with the anticipated C–C reference value[30,31]. The peak at 286.6 eV was associated with aryl carbon from the benzene ring (C–O–C), while the peak at 287.4 eV corresponds to the carboxylate carbon in O–C = O, respectively[31,32]. Turning attention to the O 1s region in Fig. 4B, the XPS spectrum exhibits three dominant peaks at 530.8 eV, 532.5 eV, and 534.0 eV, signifying Ni-O, carboxylate groups of the organic linkers, and C–O-H functionalities[30,31,33,34]. Figure 4C offers insight into the

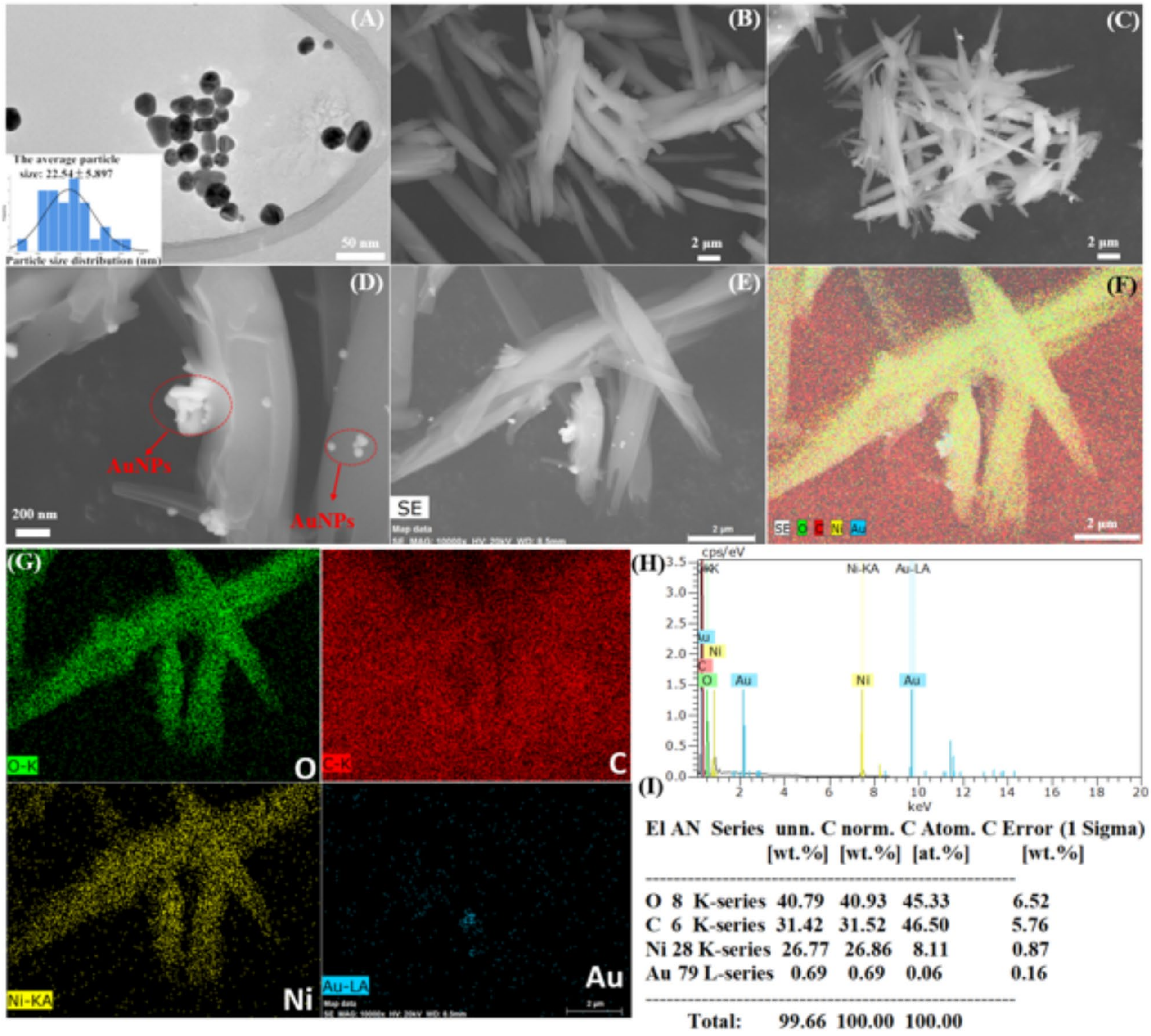

El	AN	Series	unn. C [wt.%]	norm. C [wt.%]	Atom. C [at.%]	Error (1 Sigma) [wt.%]
O	8	K-series	40.79	40.93	45.33	6.52
C	6	K-series	31.42	31.52	46.50	5.76
Ni	28	K-series	26.77	26.86	8.11	0.87
Au	79	L-series	0.69	0.69	0.06	0.16
Total:			99.66	100.00	100.00	

Fig. 2. (**A**) HR-TEM image of the AuNPs (inset: average size and size distribution of the AuNPs), SEM images of (**B**) Ni-MOF (Ni(CH_3CO_2)$_2$), (**C–E**) Au@Ni-MOF (Ni(CH_3CO_2)$_2$), (**F**,**G**) the corresponding EDS elemental mapping, and (**H**) EDX spectrum of Au@Ni-MOF (Ni(CH_3CO_2)$_2$) with the table of weight% (**I**) for the element present in the composite materials.

XPS spectrum in the Ni 2p region, where the binding energies at around 854.0 eV and 855.7 eV are attributed to Ni $2p_{3/2}$ and its satellite peaks. The binding peaks at approximately 861.2 eV and 871.5 eV are assigned to Ni $2p_{1/2}$ and its satellite peaks, respectively[31,34]. Besides, Fig. 4D provides evidence of the presence of metallic gold (Au) in the Au/Ni-MOF compound[30,32]. Two distinct peaks at 87.5 eV (Au $4f_{5/2}$) and 84.0 eV (Au $4f_{7/2}$) are consistent with the binding energy of Au 4f[35–37]. Therefore, it indicated that the expected Au@Ni-MOF (Ni(CH_3CO_2)$_2$) had been acquired.

Electrochemical behaviors of the Au@Ni-MOF (Ni(CH_3CO_2)$_2$)-modified electrodes

The CV method was used for the current response of different electrodes under the optimal conditions of 0.1 mol·L^{-1} KCl and 5.0 mmol·L^{-1} K_3[Fe $(CN)_6$] solution at a scan rate of 50 mV·s^{-1} and a potential window between −0.2 and +0.6 V. The CV currents can clearly show the response on every electrode's surface at each stage. Three redox peaks can be observed in Fig. S1A and compared with bare SPCE, Ni-MOF (Ni(CH_3CO_2)$_2$), and Au@Ni-MOF (Ni(CH_3CO_2)$_2$), which can be observed that the Au@Ni-MOF (Ni(CH_3CO_2)$_2$) (curve c) was higher than that of other electrodes (curves a and b). The possible reason is that the single layer of Au@Ni-MOF (Ni(CH_3CO_2)$_2$) formed on the electrode surface can accelerate the electron transport channel and perform the highest electrocatalytic performance and the MOFs act as a medium enhancing the ferricyanide ions approaching the electrode surface. Additionally, another useful and powerful tool is electrochemical impedance spectroscopy (EIS), which is used to study the dynamics of electron transfer and electrical conductivity on

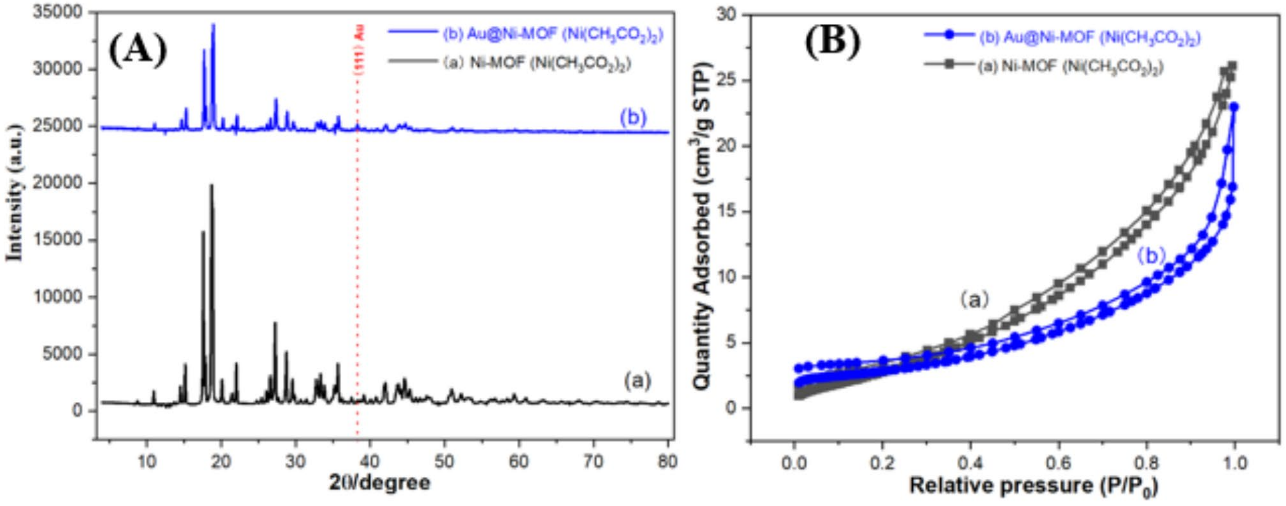

Fig. 3. (**A**) XRD patterns of Ni-MOF (Ni(CH_3CO_2)$_2$) and Au@Ni-MOF (Ni(CH_3CO_2)$_2$) and (**B**) N_2 adsorption/desorption isotherms of Ni-MOF (Ni(CH_3CO_2)$_2$) and Au@Ni-MOF (Ni(CH_3CO_2)$_2$).

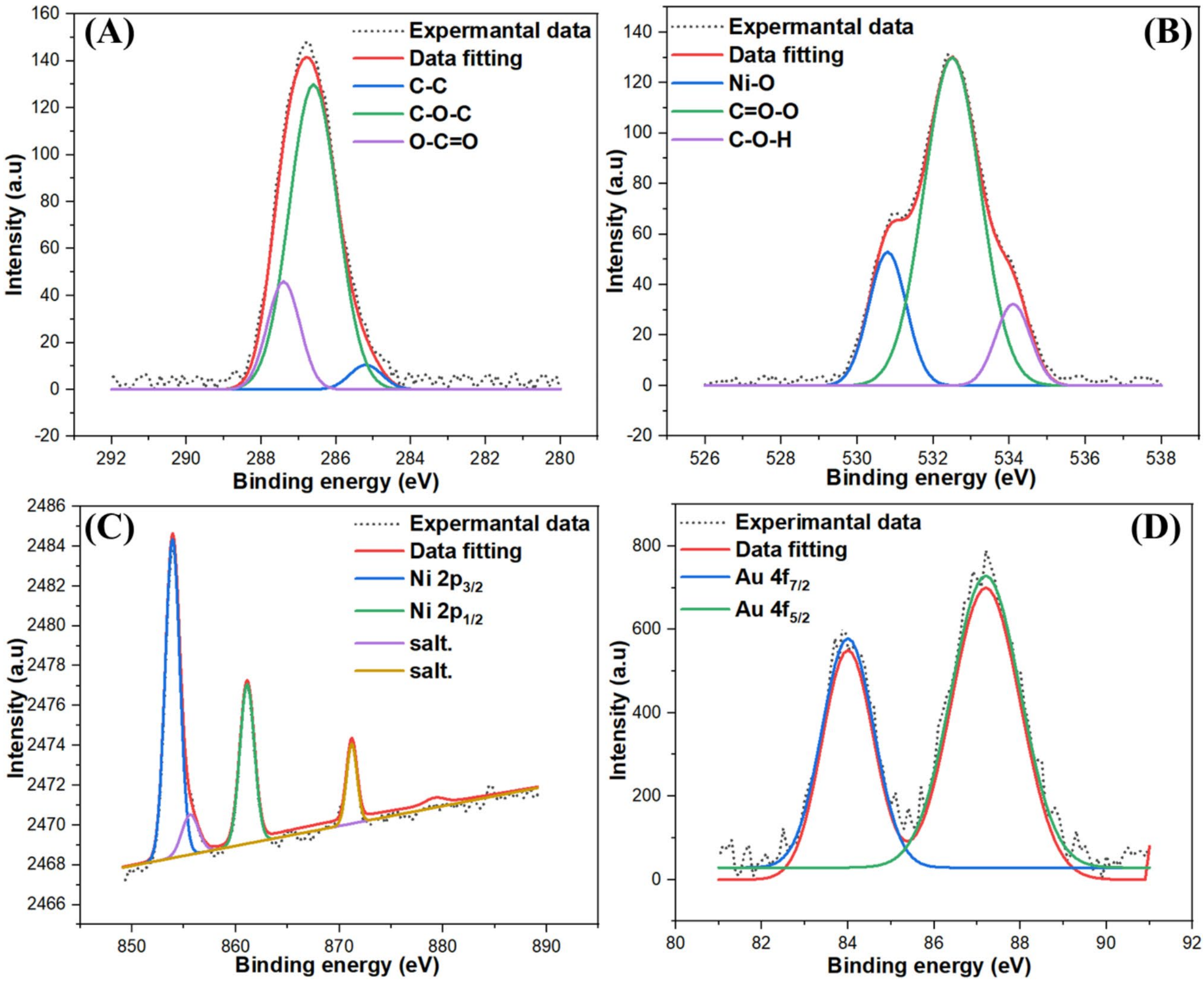

Fig. 4. XPS spectra of Au@Ni-MOF (Ni(CH_3CO_2)$_2$) in the (**A**) C 1s regions, (**B**) O 1s regions, (**C**) Ni 2p regions, and (**D**) Au regions.

the surface of electrode materials. Therefore, Fig. S1B displays the EIS spectrum of the bare SPCE, Ni-MOF ($Ni(CH_3CO_2)_2$)/SPCE, and Au@Ni-MOF ($Ni(CH_3CO_2)_2$)/SPCE. The equivalent circuit model is made up of solution resistance Rs, charge transfer resistance Rct, constant phase element (CPE) associated with the double-layer capacitance, and Warburgs impedance Zw[38]. The relationship between the slope of Nyquist plots and charge transfer resistance (Rct) was evident[39]. It was very hardly observed that the semicircle of Ni-MOF/SPCE and Au@Ni-MOF ($Ni(CH_3CO_2)_2$)/SPCE had a much lower diameter than that of bare SPCE, suggesting that these MOFs possess a faster charge transfer rate and the lowest electric resistance. This could be due to the good conductive coat of Ni-based MOFs. Moreover, the Nyquist plot of the Au@Ni-MOF ($Ni(CH_3CO_2)_2$) modified electrode displayed a more pronounced slope in the low-frequency region than the pristine Ni-based MOF electrode and the unmodified bare SPCE. This observation signifies an accelerated diffusion-controlled mass transfer in the Au@Ni-MOF ($Ni(CH_3CO_2)_2$)-modified electrode.

Furthermore, the main objective of this work is to design a green synthetic method, based on the use of trimeric acid (H_3BTC) as the organic linker source and combined with the precursor of Ni salt. It was observed that our Ni-MOF ($Ni(CH_3CO_2)_2$) could be easily synthesized at room temperature, indicating that our synthesized Ni-MOF ($Ni(CH_3CO_2)_2$) had different morphology, catalytic performance, and binding energy, as shown in Fig. 1. H_3BTC ligand could deprotonate and release protons as H^+ and BTC^{3-}, which could decrease the pH value of the solution and nickel acetate could provide the metal cation and acetate ion in an aqueous solution[40]. Acetate ions were easily combined with H^+ at low temperatures by ultrasonic method to carry out some chemical reactions to connect Ni^{2+} and BTC^{3-} to obtain Ni-based MOF: $Ni_3(BTC)_2$[40]. Therefore, the suggested synthesis of the mechanism and principle of Ni-MOF($Ni(CH_3CO_2)_2$) was described as shown in Fig. S2[41]. To the best of our knowledge, it was reported that some MOF structures existed in unsaturated metal centers (open metal sites), which could act as Lewis's acid sites and play important roles in catalytic reactions[42,43]. The MOF materials that have more open metal sites, will have a better catalytic performance[43]. Therefore, Ni-MOF ($Ni(CH_3CO_2)_2$) materials will present excellent catalytic performance, which can be obtained from the following electrochemical experiments.

Subsequently, to find a suitable optimum ratio between metals (Au and Ni) for the best electrochemical sensor performance, the electrochemical behaviors of the Au@Ni-MOF ($Ni(CH_3CO_2)_2$)/SPCE modified electrodes were investigated by CVs and DPV measurements under the conditions of 0.1 $mol \cdot L^{-1}$ KCl and 1.0 $mmol \cdot L^{-1}$ $K_3[Fe\,(CN)_6]$ solution at a scan rate of 50 mV s^{-1} and a potential window between − 0.2 and + 0.6 V. As shown in Fig. S3, 50 μM DA and UA were added in 0.01 M phosphate buffer solution (PBS, pH 6.0). An obvious phenomenon is that the anodic peak for Au@Ni-MOF ($Ni(CH_3CO_2)_2$)/SPCE (0.36 mM of AuNPs) (curve d) was higher than that of the Ni-MOF ($Ni(CH_3CO_2)_2$)/SPCE, Au@Ni-MOF ($Ni(CH_3CO_2)_2$)/SPCE (0.02 mM of AuNPs), and Au@Ni-MOF ($Ni(CH_3CO_2)_2$)/SPCE (0.12 mM of AuNPs) (curve a, b, c respectively). Therefore, with the increase of Au nanoparticles, the anodic peak was getting higher and higher for different Au@Ni-MOF ($Ni(CH_3CO_2)_2$)/SPCE electrodes. In addition, AuNPs are small in size and MOF materials have a strong adsorption capacity, so it is easier to incorporate small AuNPs inside the MOF. The high conductivity of the AuNPs to reach the surface of the material to act as an electron transmission channel further improved the conductivity of the Au@Ni-MOF ($Ni(CH_3CO_2)_2$) film. As a result, the Au@Ni-MOF ($Ni(CH_3CO_2)_2$) (0.12 mM of AuNPs) and Au@Ni-MOF ($Ni(CH_3CO_2)_2$) (0.36mM of AuNPs) catalysts were both shown to possess high electrocatalytic performance due to their high density of active sites. However, adding too many AuNPs will cause the composites to be too heavy and easy to fall off from the SPCE, and also easy to aggregate. Therefore, the Au@Ni-MOF ($Ni(CH_3CO_2)_2$)/SPCE (0.12 mM of AuNPs) was the most suitable electrochemical sensor for the simultaneous detection of DA and UA. The following experiments will all use the Au@Ni-MOF ($Ni(CH_3CO_2)_2$) (0.12 mM of AuNPs) composites to be modified SPCE.

Effect of scan rate and pH

Relevant electrode reaction kinetics between the electrochemical reaction response (oxidation peak current: I, μA) and the square root of the various potential scan rates ($v^{1/2}$, mV s^{-1}) of DA and UA are studied through conducting CV tests. It can be observed that the measured anodic peak current increases significantly in the presence of DA (Fig. 5A,C) was positive shift with the increasing scan rate (from 10 to 400 mV s^{-1}) than UA (Fig. 5B, D), suggesting the electron transfers and reaction rate of DA on the surface of the Au@Ni-MOF ($Ni(CH_3CO_2)_2$)/SPCE was better than UA. In addition, the correlation was linear with the regression equation of $I_{p.a.}(DA) = 1.339x - 6.283$ ($R^2 = 0.9887$), $I_{pc}(DA) = -\ 1.240x + 5.692$ ($R^2 = 0.9928$), and $I_{p.a.}(UA) = 1.354x - 5.493$ ($R^2 = 0.9932$) and $I_{pc}(UA) = -\ 1.167x + 5.889$ ($R^2 = 0.9947$), suggesting two adsorption-controlled processes or electron transfer occurred on Au@Ni-MOF ($Ni(CH_3CO_2)_2$)/SPCE (Fig. 5B,D, respectively). Additionally, the amalgamation of the substantial surface area inherent to Ni-based MOFs and the heightened conductivity of AuNPs, characterized by synergistic effects, conferred advantageous attributes for the adsorption of diminutive biomolecules onto the electrode's surface. Furthermore, the electrooxidation of DA and UA at the Au@Ni-MOF ($Ni(CH_3CO_2)_2$) electrode resulted in a more efficient electron transfer process. This efficacy can be attributed to the electrode's enhanced electrochemical catalytic performance, stemming from its elevated conductivity and expansive surface area.

More generally, pH is an important factor affecting the electrochemical performance of many sensors and the pH of the electrolyte medium can affect the kinetics and thermodynamics of the electron transfer process[15]. Therefore, it is vital to investigate the pH effects and to find the optimal pH value for the detection of DA and UA. The electrochemical behavior of DA (50 μM) and UA (50 μM) was studied by CV measurement at a scan rate of 50 mV s^{-1} in 0.01 M PBS at different pH values (3 to 10) in a given potential range of − 0.2–0.6 V, as shown in Fig. 6A,C. When the hydrogen ions decreased in the electrolyte solution, the oxidation peaks current (Ipa) value slowly increased in the range of PH from 3.0 to 6.0, and then sharply decreased within the pH from 6.0 to 10.0, indicating that protons transport plays an important role in the electrochemical reactions, accompanied

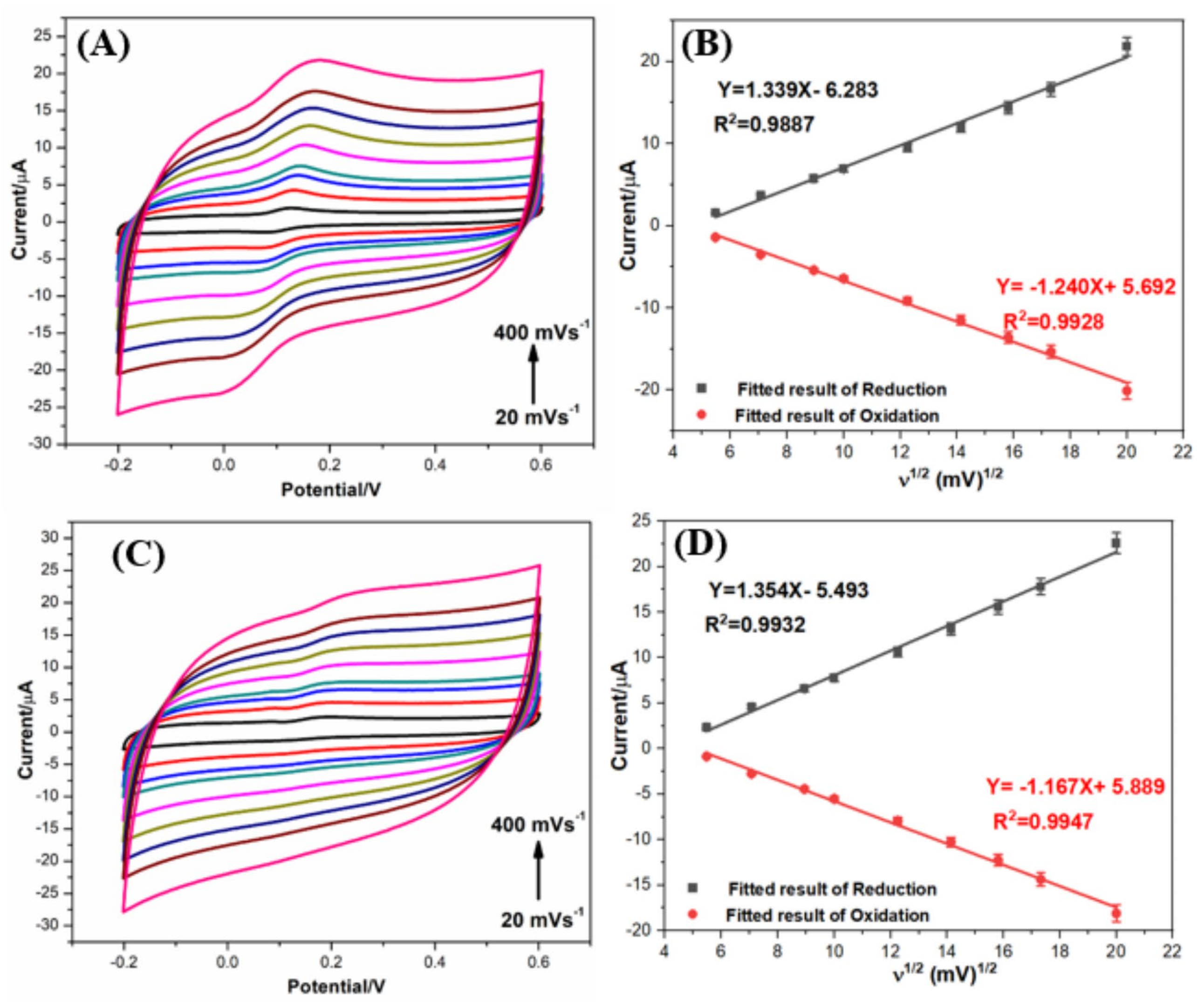

Fig. 5. CVs for the oxidation of 50 μM (**A**) DA and (**C**) UA at Au@Ni-MOF ($Ni(CH_3CO_2)_2$)/SPCE in 0.01 M PBS at different scan rates from 20 to 400 mV·s^{-1}, (**B**) DA and (**D**) UA of the linear dependence of the reduction peak current and oxidation peak current on the square root of the scan rate.

by proton release and capture[15,44]. In addition, when the electrolyte solution has too many hydrogen ions, the oxidation peak potential (Epa) of DA and UA both shift from positive to negative with the increase of pH from 3.0 to 10.0, which were in complete agreement with the results of previous studies[12,45,46]. At the same time, Nafion has been frequently used as a binder will lead to different results at different pH values. Nafion has anionic sulfonic acid groups that can attract ammonium cation converted from DA, which is conducive to DA adsorption and permeation. If the pH values are too low, the proton can interact with the sulfonate group instead of the ammonium cation to hinder DA adsorption and permeation. However, when the pH values are too high, DA may happen to deprotonate in the hydroxyl group, and then suffer a negative charge[15]. Therefore, it is unbeneficial for DA adsorption and permeation under the conditions of too low pH or too high pH. At last, the two types of Au@Ni-MOF ($Ni(CH_3CO_2)_2$) exhibited the highest peak current at an intermediate value of pH 6.0 (Fig. 6B,D), which was used as an optimal pH for the detection of DA and UA.

Individual and simultaneous determination of DA and UA

Additionally, the DPV method is used for the DA and UA sensing process. Different concentrations of DA and UA were measured separately by this electrochemical sensor under the conditions of 0.01 M PBS (pH 6.0) at a scan rate of 50 mV s^{-1}. To obtain a higher sensitivity and linear range under the optimum conditions, a series of experiments were carried out and many good results were demonstrated. As depicted in Fig. 7A,C, it can be observed that the DPV curve responds to the individual and simultaneous detection of enhanced DA and UA concentrations on Au@Ni-MOF ($Ni(CH_3CO_2)_2$)/SPCE, and the oxidation peak currents increased sequentially with the increase of the concentration of each species. Furthermore, all the oxidation peaks showed relatively small increasing red-shifting as the concentration of DA and UA increased. When the DA or UA level was changed from 0 to the maximum, the oxidation peak potentials at the Au@Ni-MOF ($Ni(CH_3CO_2)_2$)/

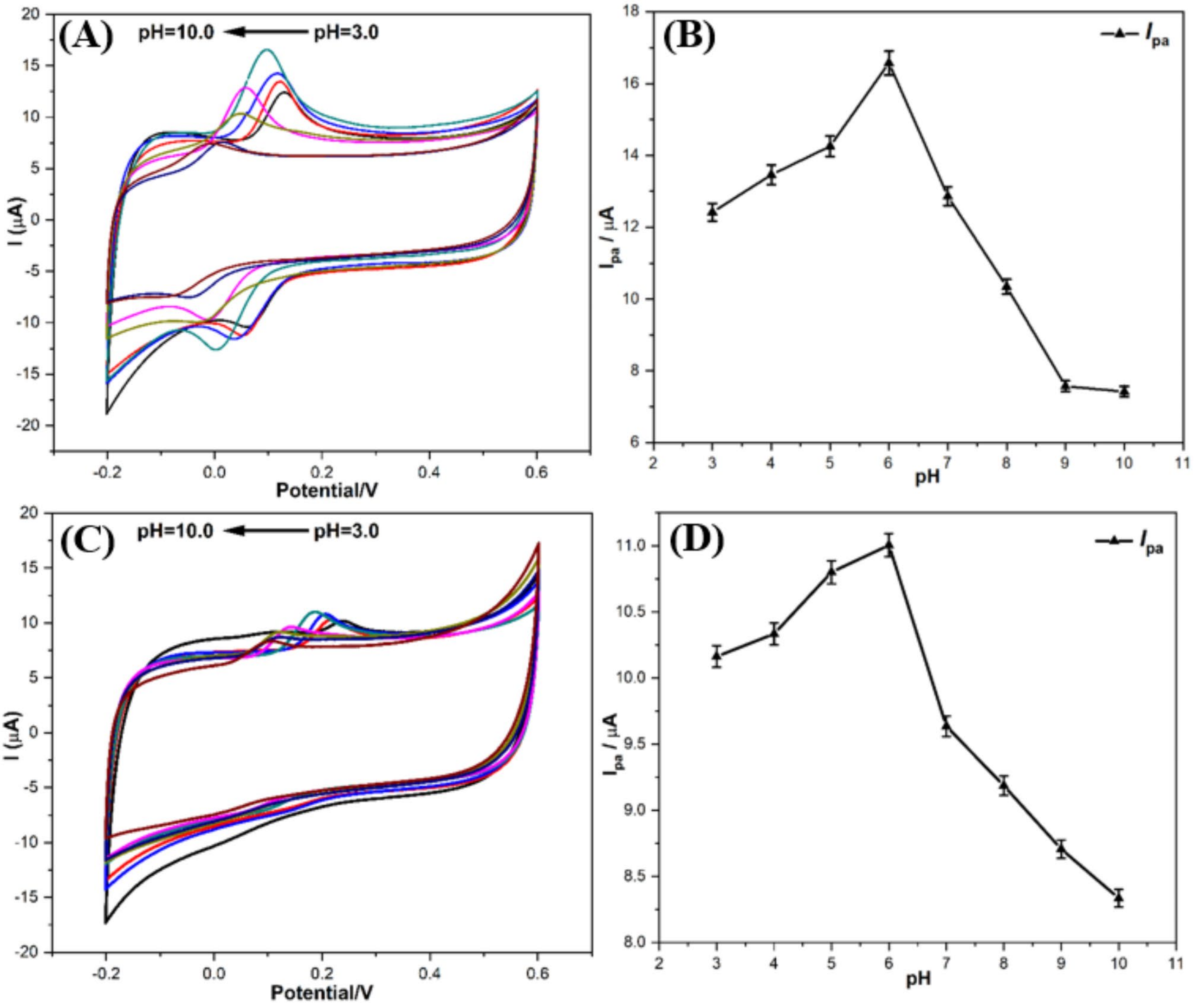

Fig. 6. The effect of pH on the current response of 50 μM DA (**A**) and UA (**C**) at Au@Ni-MOF ($Ni(CH_3CO_2)_2$)/SPCE at a scan rate of 50 mV s^{-1}; Plot of oxidation peak current (Ipa) and oxidation peak potential (Epa) of DA (**B**) and UA (**D**) versus pH.

SPC electrode shifted to the right by about 355.2 mV and 191.3 mV, respectively. Regardless of the DA or UA detection, the peak potential separation of the Au@Ni-MOF ($Ni(CH_3CO_2)_2$)/SPC electrode showed excellent electrocatalytic activities and electroconductibility. The reasons may be as follows: (1) H_3BTC ligands in Au@Ni-MOF ($Ni(CH_3CO_2)_2$) composites with complete or partial deprotonation may interact with the target molecules via hydrogen bonding, and/or electrostatic interactions, which can activate the multi-carboxylate groups and accelerate the charge transfer kinetics of the target analytes at the Au@Ni-MOF ($Ni(CH_3CO_2)_2$) materials[47–49]; (2) Au@Ni-MOF ($Ni(CH_3CO_2)_2$) composite has a particularly high surface area and small pore-size distribution, which are easier for fast electron transfer of DA and UA in aqueous electrolyte[23].

Additionally, the electrocatalytic peak current density of the electrodes was linearly related to the concentrations of DA and UA, the widely linear range for the individual analysis of each substance was 0.1 μM to 2 mM (DA) and 0.5 μM to 1.5 mM (UA) for Au@Ni-MOF ($Ni(CH_3CO_2)_2$)/SPCE sensor. According to the description of Fig. 7B,D, when the Au@Ni-MOF ($Ni(CH_3CO_2)_2$)/SPCE sensor separate analysis of the target molecules, the different linear calibration equations for each species were $I_{DA}(\mu A) = 0.0935C_{DA}(\mu M) + 0.914$ ($R^2 = 0.9917$), $I_{DA}(\mu A) = 0.0221C_{DA}(\mu M) + 8.562$ ($R^2 = 0.9601$) and $I_{DA}(\mu A) = 0.0122C_{DA}(\mu M) + 17.15$ ($R^2 = 0.9949$) within three successively increasing concentration ranges between 0.1 and 80 μM, 80–1000 μM and 1000–2000 μM as well as $I_{UA}(\mu A) = 0.1189C_{UA}(\mu M) + 3.465$ ($R^2 = 0.9968$) and $I_{UA}(\mu A) = 0.0098C_{UA}(\mu M) + 8.289$ ($R^2 = 0.9933$) within two successively increasing concentration ranges between 0.5 and 30 μM and 50–1500 μM, respectively. In addition, in the different linear ranges for the electrochemical sensing of DA and UA on Au@Ni-MOF ($Ni(CH_3CO_2)_2$)/SPCE, the smallest low detection limits (LODs) were calculated to be approximately 0.06 μM and 0.05 μM ($S/N = 3$), with the highest sensitivity of 0.85 μA mM^{-1} mm^{-2} and 1.08 μA mM^{-1} mm^{-2}, respectively.

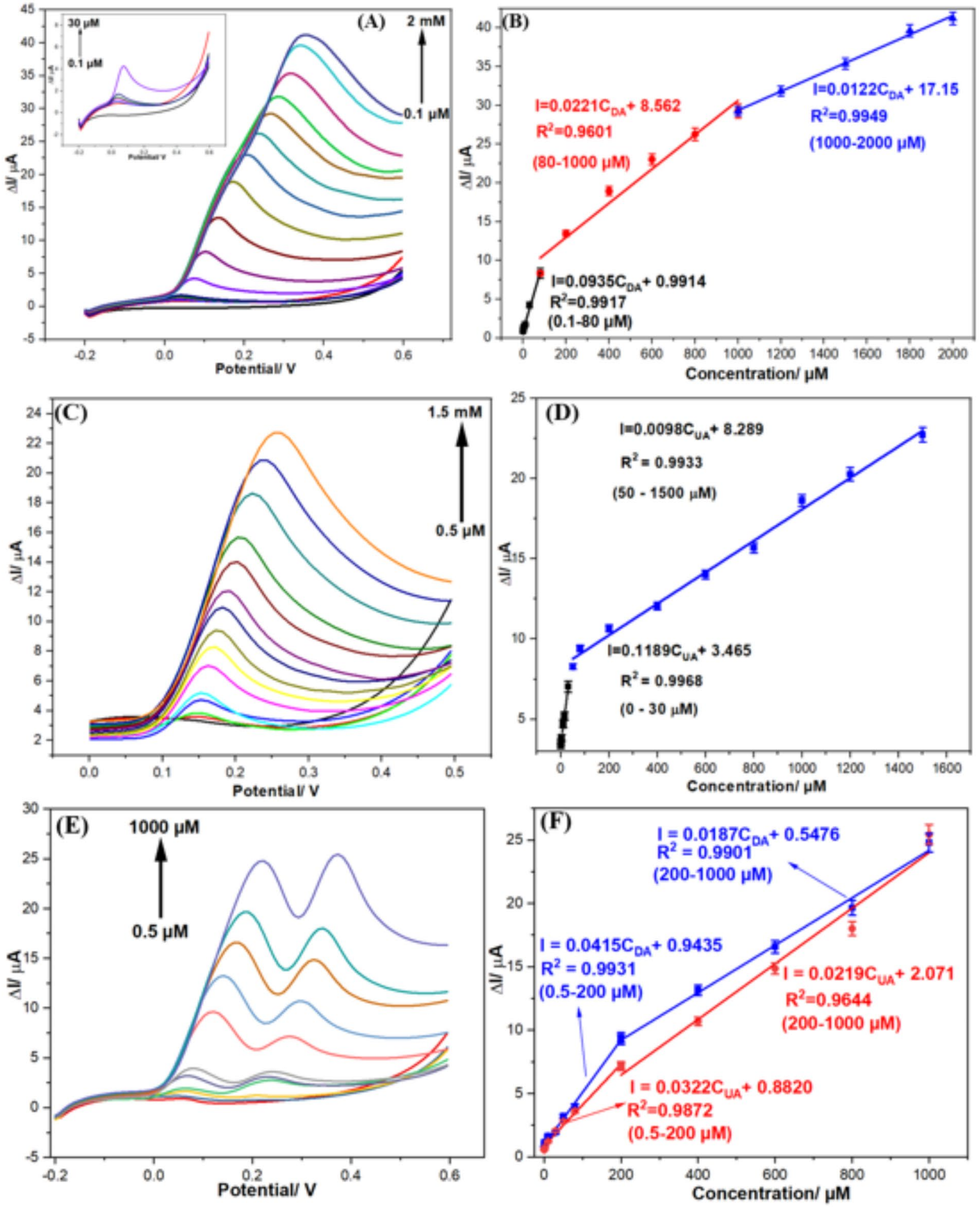

Fig. 7. (**A**) DPV of DA with increasing concentration from 0.1 μM to 2 mM (inset dependence of peak current for DA with increasing concentration from 0.1 μM to 30 μM) and (**B**) The relationship of the calibration curve of ΔI with the concentration (μM) of DA at a scan rate of 50 mV s^{-1} for Au@Ni-MOF (Ni(CH$_3$CO$_2$)$_2$) electrode; (**C**) DPV of UA with increasing concentration from 0.5 μM to 1.5 mM and (**D**) The relationship of the calibration curve (ΔI/A) with the concentration (μM) of UA at a scan rate of 50 mV·s^{-1} for Au@Ni-MOF (Ni(CH$_3$CO$_2$)$_2$) electrode; (**E**) DPV of the simultaneous detection DA and UA with increasing concentration from 0.5 μM to 1000 μM and (**F**) The relationship of the calibration curve of ΔI with the concentration of DA and UA at a scan rate of 50 mV·s^{-1} for Au@Ni-MOF (Ni(CH$_3$CO$_2$)$_2$) electrode.

What's more, DPV measurement has higher sensitivity and better resolution than the CV method, so it is a wise choice to use the DPV technique for the simultaneous determination of DA and UA at the Au@Ni-MOF ($Ni(CH_3CO_2)_2$) electrodes. As depicted in Fig. 7E,F, it can be observed that with the increasing concentration of each analyte, the electro-oxidation peaks changed from initially without any peaks to two weak and poorly shaped peaks, and further to an increasingly pronounced doublet peak, until finally the doublet peaks become more and more pronounced. Moreover, for the Au@Ni-MOF ($Ni(CH_3CO_2)_2$)/SPCE sensor (Fig. 7F), the achieved electrocatalytic peak currents had two linear relationships with the DA and UA concentration within the ranges of 0.5–1000 μM. Certainly, it had different linear equations in different concentration range, and the linear regression equations were calibrated as $I_{DA}(\mu A) = 0.0415C_{DA}(\mu M) + 0.9435$ ($R^2 = 0.9931$) and $I_{UA}(\mu A) = 0.0322C_{UA}(\mu M) + 0.8820$ ($R^2 = 0.9872$) between 0.5 and 200 μM, another two equations were obtained as $I_{DA}(\mu A) = 0.0187C_{DA}(\mu M) + 0.5476$ ($R^2 = 0.9901$) and $I_{UA}(\mu A) = 0.0219C_{UA}(\mu M) + 2.071$ ($R^2 = 0.9644$) between 200 and 1000 μM. Moreover, the smallest LOD values and the highest sensitivity for DA and UA in small concentration ranges were calculated at about 0.14 μM and 0.19 μM as well as 0.38 $\mu A\ \mu M^{-1}\ cm^{-2}$ and 0.29 $\mu A\ \mu M^{-1}\ cm^{-2}$, respectively. These good results demonstrate that simultaneous determination of DA and UA can be achieved with high sensitivity and selectivity at the Au@Ni-MOF ($Ni(CH_3CO_2)_2$) electrode. On the other hand, whether it was detected individually or simultaneously, the Au@Ni-MOF ($Ni(CH_3CO_2)_2$)/SPCE sensor showed small LOD and high sensitivity, suggesting that Au@Ni-MOF ($Ni(CH_3CO_2)_2$) hybrids could present excellent electrocatalytic performance and the ability to transfer electrons. Furthermore, in cooperation with other materials reported in the literature for the simultaneous determination of DA and UA (Table 1), the Au@Ni-MOF ($Ni(CH_3CO_2)_2$) composites exhibited good results as promising electrode materials for electrochemical sensing. Besides, it can be observed that the important analytical parameter of the linear ranges for the Au@Ni-MOF ($Ni(CH_3CO_2)_2$)/SPC electrode is superior to or comparable to so far reported papers for the individual and simultaneous determination of the two small targets biomolecules. To our knowledge, few reports had direct electrochemical determination of DA and UA in coexistence systems by using MOF-based composites as electrode modifiers, especially via using the MOF-metal particle composites developed in our work to modify the electrodes. At the same time, they are also two very innovative and promising materials as electrodes in the field of electrochemistry. In addition, the Au@Ni-MOF ($Ni(CH_3CO_2)_2$) materials offer remarkable practical significance and novelty in DA and UA detection. In comparison to other sensor materials, the unique structure of Au@Ni-MOF ($Ni(CH_3CO_2)_2$) provides a synergistic effect. The presence of gold nanoparticles within the Ni-MOF framework not only enhances the conductivity but also offers catalytic active sites. This leads to a significant improvement in electron transfer kinetics, which is directly reflected in the higher sensitivity and lower limit of detection we have obtained. For instance, in contrast to some commonly used carbon-based sensor materials, our Au@Ni-MOF ($Ni(CH_3CO_2)_2$) composites show a more pronounced electrocatalytic activity towards DA and UA oxidation, allowing for more accurate and reliable detection even at low analyte concentrations. Moreover, the stability and reproducibility of our material in complex biological samples outperform many traditional sensor materials, making it more suitable for practical applications.

Density functional theory (DFT) simulation

The optimizations of the molecular structures in the study were conducted employing Density Functional Theory (DFT), a widely employed quantum mechanical method for calculating electronic properties of molecules and materials. The calculations were executed using the DMol3 module, a computational tool incorporated within the Material Studio software[38,57]. For the systems under investigation, which encompassed DA and UA, the electron density and molecular orbitals were computed. The obtained results, as illustrated in Fig. S4, are presumably pivotal for understanding the electronic structure and reactivity of these molecules.

Moreover, computational chemistry techniques play a pivotal role in elucidating the biological activity of specific molecules, complemented by an abundance of theoretical investigations aimed at discerning their chemical reactivity[58]. In electronic structure theory, the Highest Occupied Molecular Orbital (HOMO) is the molecular orbital with the highest energy, while the Lowest Unoccupied Molecular Orbital (LUMO) has the lowest energy. The energy gap between these two orbitals, known as the HOMO-LUMO gap or Eg, represents the minimum energy required to move an electron from the HOMO to the LUMO[57–60]. HOMO-LUMO

		Linear range (μM)		Low detection limit (μM)		
Electrode material	**Methods**	**DA**	**UA**	**DA**	**UA**	**References**
Fe-MOF/GCE	DPV	10–90	10–90	3.33	3.27	[50]
Ni-ZIF-8/N S-CNTs/CS/GCE	DPV	8–500	1–600	0.93	0.41	[51]
Au@Cu-MOF	DPV	10-1000	10–1000	3.40	10.36	[52]
HNP-PtTi/GCE	DPV	4–500	100–1000	3.2	5.3	[53]
$ZnCl_2$-CF/GCE	DPV	10–330	10–250	10	10	[54]
MWCNTs/GCE	CV	5–120	5–120	4.5	1.5	[55]
Graphene oxide-ZIF67/GCE	DPV	40–2330	40–415	26.2	8.0	[56]
Au@Ni-MOF ($Ni(CH_3CO_2)_2$)/SPCE	DPV	0.5–1000	0.5–1000	0.14	0.19	This work

Table 1. Comparison of the electroanalytic performances for the simultaneous determination of DA and UA indifferent electrode materials.

determination and its other several important key factors for conductivity activity which as energy gap (ΔE_g), hardness (η), softness (σ), and the global electronegativity (χ) were calculated by using Eqs. (1)–(4)[58–60], as shown in Table S2.

$$E_g = E_{LUMO} - E_{HOMO} \tag{1}$$

$$\eta = \frac{E_{LUMO} - E_{HOMO}}{2} \tag{2}$$

$$\sigma = \frac{1}{\eta} \tag{3}$$

$$\chi = -\frac{E_{LUMO} + E_{HOMO}}{2} \tag{4}$$

Based on the data presented in Fig. S4 and Table S2, it is evident that UA has a smaller HOMO-LUMO gap value compared to DA. A smaller value of this descriptor indicates higher molecular activity[58]. This discrepancy suggests that DA is more favorable for electron excitation, potentially enhancing electrical conductivity. Furthermore, an increase in softness and a decrease in hardness values are associated with increased biological activity[58]. Based on the hardness (η) and softness (σ) values of DA and UA, it is evident that UA has a better softness than DA, indicating that UA is much more active than DA. Another important parameter is global electronegativity (χ). Global electronegativity is associated with the electron's freedom within a molecule. A lower electronegativity value signifies that electrons within the molecule are more mobile compared to other molecules. Inhibitors typically coordinate with suitable acceptor molecules by donating electrons. As a result, biological activity increases as the global electronegativity value decreases[58]. According to their global electronegativity values, DA exhibits higher activity than UA.

Additionally, the adsorption energy or interaction energy, E_{ads}, was determined using Eq. (5)[57].

$$E_{ads} = E_{complex} - (E_{substrate} + E_{adsorbate}) \tag{5}$$

In this equation, "E_{ads}" represents the adsorption energy, and "$E_{complex}$" signifies the total energy of the complex formed after the adsorption of the target analytes (DA and UA) onto the surfaces of Ni-MOF ($Ni(CH_3CO_2)_2$) or Au@Ni-MOF ($Ni(CH_3CO_2)_2$). "$E_{substrate}$" and "$E_{adsorbent}$" correspond to the individual energies of the target analytes and the Ni-MOF ($Ni(CH_3CO_2)_2$) or Au@Ni-MOF ($Ni(CH_3CO_2)_2$) materials, respectively. Furthermore, as illustrated in Fig.S5 and detailed in Table S3, the adsorption energy for two DA molecules was notably higher at – 536.63 kJ/mol in comparison to the scenario where two UA molecules were adsorbed or when one DA and one UA interacted, yielding an energy of – 404.95 kJ/mol and – 434.74 kJ/mol, respectively. It is worth highlighting that the adsorption energy of Au@Ni-MOF ($Ni(CH_3CO_2)_2$), when both DA and UA were involved, surpassed that of Ni-MOF ($Ni(CH_3CO_2)_2$) in isolation. This indicates that the incorporation of AuNPs resulted in an overall increase in energy and an enhancement of the adsorption energy for specific small biomolecules. These observations strongly imply that DA exhibits a significantly stronger adsorption affinity for the surface of both Ni-MOF ($Ni(CH_3CO_2)_2$) and Au@Ni-MOF ($Ni(CH_3CO_2)_2$) composites in comparison to UA. Consequently, UA can be more swiftly adsorbed onto Au@Ni-MOF ($Ni(CH_3CO_2)_2$)/SPCE with a higher affinity, leading to LOD for DA as opposed to UA. In summary, the Au@Ni-MOF ($Ni(CH_3CO_2)_2$)/SPCE sensor is anticipated to demonstrate superior capabilities in detecting DA when compared to UA, aligning with the findings presented in Fig. 7.

Reproducibility, stability, and selectivity

Subsequently, the reproducibility test of the Au@Ni-MOF ($Ni(CH_3CO_2)_2$)/SPCE sensors was further investigated by DPV technology under optimal conditions when 50 µM DA and 150 µM UA were added at the same time, as shown in Fig. 8A,B. The relative standard deviations (RSDs) of the electrode responses to DA and UA twenty times by using two different electrodes in the DPV curves were calculated at 0.32% and 1.38%, respectively. From the above computational results, we can deduce that the Au@Ni-MOF ($Ni(CH_3CO_2)_2$)/SPCE sensor could show outstanding reproducibility, suggesting that the small changes can be ignored by using different electrodes for the simultaneous detection of DA and UA. Furthermore, it is shown that the Au@Ni-MOF ($Ni(CH_3CO_2)_2$)/SPCE sensor has a lower value for the detection of DA than UA, demonstrating that the Au@Ni-MOF ($Ni(CH_3CO_2)_2$) material can exhibit excellent electrocatalytic performance and carry out much electron transfer in the detection process.

For better comparison, we also carried out some experiments to check the stability of the resulting sensor system for simultaneous determination of DA and UA. As shown in Fig. 8C,D, when the electrodes were stored at room temperature for one week, the electrocatalytic current displayed only a small decrease after 600 cycles of CV tests. Among, DA and UA decreased by 1.56%, and 1.16% for the Au@Ni-MOF ($Ni(CH_3CO_2)_2$) electrode, respectively. On the other hand, to study the selectivity of the electrochemical sensor for DA and UA detection, various possible interferences were investigated, including glucose, urea, NaCl, $NaNO_3$, NaF, $CaCl_2$, $ZnSO_4$, and ascorbic acid. As shown in Fig. 8E,F, each kind of interference (50 µM) was investigated by DPV measurements in the presence of 50 µM DA and UA at a scan rate of 50 mV s^{-1} in 0.01 M PBS solution. These results demonstrated that the peak currents of DA and UA oxidation don't produce remarkable changes after adding these interfering species one by one. Moreover, Fig. 8 demonstrated that the average current change for Au@Ni-MOF ($Ni(CH_3CO_2)_2$) electrodes was 1.3% and 2.9%, and their relative standard deviations were calculated to be about 0.8% for DA and 2% for UA, respectively. We can observe that the Au@Ni-MOF ($Ni(CH_3CO_2)_2$)/

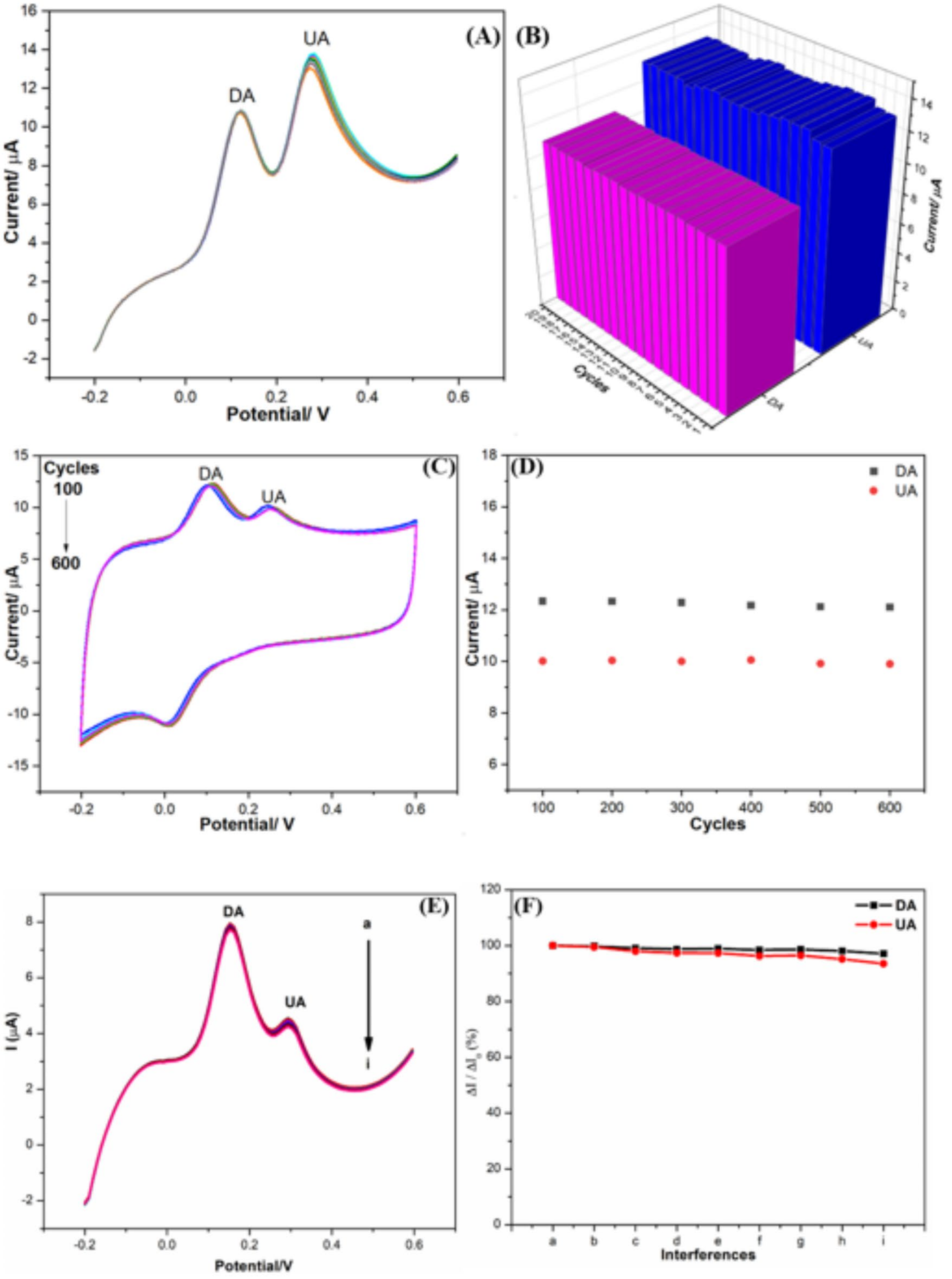

Fig. 8. (**A**) The CVs values for evaluating the reproducibility of simultaneous detection of 50 µM DA and 150 µM UA; (**B**) The current vs. cycles of Au@Ni-MOF ($Ni(CH_3CO_2)_2$)/SPCE for evaluating the reproducibility of simultaneous detection of target analytes in concentrations of 50 µM DA and 150 µM UA; (**C**) CVs obtained after 600 cycles for Au@Ni-MOF ($Ni(CH_3CO_2)_2$) modified electrodes in 0.01 M PBS (pH = 6) solution containing 50 µM DAand 30 µM UA at a scan rate of 50 $mV \cdot s^{-1}$, (**D**) The peak currents collected after 600-cycle CVs run in 0.01 M PBS (pH = 6) solution containing 50 µM DA and UA; (**E**) The DPV curve at Au@Ni-MOF ($Ni(CH_3CO_2)_2$) modified electrode in 0.01 M PBS (pH 6.0) in the presence of 50 µM DA and 30 µM UA without any interference(curve a) and with same concentrations of (b) glucose, (c) urea, (d) NaCl, (e) $NaNO_3$, (f) NaF, (g) $CaCl_2$, (h) $ZnSO_4$, (i) ascorbic acid. (**F**) The relationship of these interference current curves of (ΔI) relative to DA and UA (ΔI_0) at a scan rate of 50 $mV \cdot s^{-1}$ for Au@Ni-MOF ($Ni(CH_3CO_2)_2$) electrode.

	Found (µM)		Recovery (%)		RSD (%)	
Concentration (µM)	**DA**	**UA**	**DA**	**UA**	**DA**	**UA**
Serum						
0	–	–	–	–	–	–
50	49.55	49.04	99.10	98.08	3.57	5.34
100	99.21	98.69	99.21	98.69	2.58	6.44
Urine						
0	–	–	–	–	–	–
50	49.19	48.76	98.38	97.52	3.58	4.30
100	101.00	92.50	101.00	92.50	2.87	5.05

Table 2. The recoveries of DA and UA at Au@Ni-MOF (Ni(CH_3CO_2)$_2$)/SPCE from human serum and human urine samples with a standard addition method (each sample was tested three times).

SPCE sensor displayed surpassingly selective and sensitive detection of DA and UA due to the huge surface area, high conductivity, and excellent electrocatalytic performance of Au@Ni-MOF (Ni(CH_3CO_2)$_2$) composite. Thus, these good results strongly illustrated that the proposed electrochemical sensor based on the Au@Ni-MOF (Ni(CH_3CO_2)$_2$) can present excellent reproducibility and stability, high anti-interference ability as well as transcendently selective and sensitive capability towards the DA and UA determination.

Real samples analysis

To further assess the practicality of the electrochemical biosensor, we conducted simultaneous detection of DA and UA in human serum and urine samples on an Au@Ni-MOF (Ni(CH_3CO_2)$_2$)/SPCE platform. Before detection, the serum and urine samples were diluted 200-fold with a 0.01 M PBS solution at a pH of 6.0 to minimize interference from other components. Employing a standard spiked method, known concentrations of DA and UA were introduced into the diluted serum and urine samples to verify their concentrations. These concentrations were determined by using the standard curves presented in Fig. 7E. As shown in the results presented in Table 2, the spike recoveries fell within the range of 98.08–101%, with a relative standard deviation (RSD) ranging from 2.58 to 6.44% as obtained from three parallel experiments. These findings indicate the high reliability, sensitivity, and resolution of the Au@Ni-MOF (Ni(CH_3CO_2)$_2$)/SPCE biosensor in the context of DA and UA sensing within real samples.

Conclusion

This study comprehensively explores conductive Ni-based metal-organic frameworks as effective electrocatalysts for electrochemical detection of dopamine (DA) and uric acid (UA) in aqueous solutions. The remarkable performance of the Au@Ni-MOF (Ni(CH_3CO_2)$_2$)/SPCE biosensor in the electrochemical detection of DA and UA is intrinsically linked to the unique characteristics of the Au@Ni-MOF material. Firstly, the high sensitivity of the biosensor can be attributed to the synergistic effect of the Ni-MOF (Ni(CH_2CO_2)$_2$) and AuNPs. The Ni-MOF provides a large surface area and abundant active sites, facilitating the adsorption of DA and UA. The incorporated AuNPs enhance the electron transfer kinetics, allowing for a more efficient conversion of the electrochemical signal. This combination enables the detection of even trace amounts of DA and UA, leading to a high sensitivity.

The newly developed Au@Ni-MOF (Ni(CH_3CO_2)$_2$)/SPCE biosensor demonstrates remarkable attributes, including high sensitivity, low limits of detection (LODs), broad linear detection ranges, exceptional resistance to interference, and excellent reproducibility for DA and UA detection. The remarkable performance of the Au@Ni-MOF (Ni(CH_2CO_2)$_2$)/SPCE biosensor in the electrochemical detection of DA and UA is intrinsically linked to the unique characteristics of the Au@Ni-MOF material. Firstly, the high sensitivity of the biosensor can be attributed to the synergistic effect of the Ni-MOF (Ni(CH_2CO_2)$_2$) and AuNPs. The Ni-MOF provides a large surface area and abundant active sites, facilitating the adsorption of DA and UA. The incorporated AuNPs enhance the electron transfer kinetics, allowing for a more efficient conversion of the electrochemical signal. This combination enables the detection of even trace amounts of DA and UA, leading to a high sensitivity. Regarding the low limits of detection, the strong adsorption capabilities of the Au@Ni-MOF towards DA and UA, as evidenced by the substantial adsorption energies, play a crucial role. The AuNPs contribute to reducing the background noise and improving the signal-to-noise ratio. This means that the biosensor can detect very low concentrations of the analytes, achieving a low LOD. The broad linear detection range is a result of the stable and consistent electrochemical behavior of the Au@Ni-MOF. The Ni-MOF's stable structure and active sites ensure a reliable response over a wide range of analyte concentrations. The AuNPs help to maintain the linear relationship between the detected signal and the analyte concentration by optimizing the electron transfer process. The exceptional resistance to interference is due to the selective adsorption and reactivity of the Au@Ni-MOF. The material has a specific affinity for DA and UA, while minimizing the interactions with interfering substances. The AuNPs may also modify the surface properties of the electrode, further enhancing its selectivity and reducing interference. The excellent reproducibility is related to the uniform and stable synthesis of the Au@Ni-MOF. The controlled synthesis process ensures that each biosensor fabricated with the Au@Ni-MOF has similar electrochemical properties, leading to consistent detection results.

Additionally, through density functional theory (DFT) simulations, it was revealed that UA exhibits greater reactivity than DA. The substantial adsorption energies observed for both DA and UA on the surfaces of Ni-MOF ($Ni(CH_3CO_2)_2$) and Au@Ni-MOF ($Ni(CH_3CO_2)_2$) indicate the robust adsorption capabilities of the synthesized Ni-MOF material. In the final analysis, the Au@Ni-MOF ($Ni(CH_3CO_2)_2$)/SPCE biosensor demonstrated its applicability by successfully detecting DA and UA in authentic serum and urine samples. These findings underscore the potentiality of this biosensor for future applications, holding promise for the field of electrochemical sensing and biosensing in real-world scenarios.

Data availability

The datasets used and/or analysed during the current study available from the corresponding author on reasonable request.

Received: 11 October 2024; Accepted: 7 February 2025

References

1. Qu, Z. et al. Designing C-Fe-O bonded MIL-88B(Fe)/jasmine petal-derived-carbon composite biosensor for the simultaneous detection of dopamine and uric acid. *Chem. Eng. J.* **404**, 126570 (2021).
2. Xu, F., Wang, L., Wu, M. & Ma, G. Vertical growth of leaf-like co-metal organic framework on carbon fiber cloth as integrated electrode for sensitive detection of dopamine and uric acid. *Sens. Actuators B Chem.* **386**, 133734 (2023).
3. Krishnan, S., Tong, L., Liu, S. & Xing, R. A mesoporous silver-doped TiO_2-SnO_2 nanocomposite on g-C_3N_4 nanosheets and decorated with a hierarchical core-shell metal-organic framework for simultaneous voltammetric determination of ascorbic acid, dopamine and uric acid. *Microchim. Acta.* **187**, 82 (2020).
4. Azizpour Moallem, Q. & Beitollahi, H. Electrochemical sensor for simultaneous detection of dopamine and uric acid based on a carbon paste electrode modified with nanostructured Cu-based metal-organic frameworks. *Microchem. J.* **177**, 107261 (2022).
5. Chen, C. et al. A novel dopamine electrochemical sensor based on a β-cyclodextrin/Ni-MOF/glassy carbon electrode. *Microchem. J.* **194**, 109328 (2023).
6. Xie, W. et al. Label-free and highly selective MOFs-based dopamine detection in urine of Parkinson's patients. *Chem. Eng. J.* **443**, 136371 (2022).
7. Feng, Z. et al. Enhanced simultaneous voltammetric detection of dopamine and uric acid using Au@Ni-metal–organic framework-modified electrode. *Appl. Organomet. Chem.* **7350** (2024).
8. Feng, Z., Lim, H. N., Ibrahim, I. & Gowthaman, N. S. K. A review of zeolitic imidazolate frameworks (ZIFs) as electrochemical sensors for important small biomolecules in human body fluids. *J. Mater. Chem. B.* **11**, 9099–9127 (2023).
9. Nangare, S. N. et al. Surface architectured metal organic frameworks-based biosensor for ultrasensitive detection of uric acid: recent advancement and future perspectives. *Microchem. J.* **169**, 106567 (2021).
10. Ahmad, M. W., Dey, B., Sarkhel, G., Yang, D. J. & Choudhury, A. Sea-urchin-like cobalt-MOF on electrospun carbon nanofiber mat as a self-supporting electrode for sensing of xanthine and uric acid. *J. Electroanal. Chem.* **920**, 116646 (2022).
11. Zhao, Z. et al. Area-selective and precise assembly of metal organic framework particles by atomic layer deposition induction and its application for ultra-sensitive dopamine sensor. *Nano Today*. **42**, 101347 (2022).
12. Chen, S. et al. N-doped Cu-MOFs for efficient electrochemical determination of dopamine and sulfanilamide. *J. Hazard. Mater.* **390**, 122157 (2020).
13. Arthanari, S. R. S. et al. Fabrication of porous non-enzymatic glucose sensing electrodes through nanosecond-laser patterning of Metal-Organic frameworks. *Adv. Mater. Technol.* **9**, 2301561 (2024).
14. Huang, Z., Zhang, L., Cao, P., Wang, N. & Lin, M. Electrochemical sensing of dopamine using a Ni-based metal-organic framework modified electrode. *Ionics* **27**, 1339–1345 (2021).
15. Gao, L. L. & Gao, E. Q. Metal-organic frameworks for electrochemical sensors of neurotransmitters. *Coord. Chem. Rev.* **434**, 213784 (2021).
16. Radhakrishnan, S. S. C., Ko, T. H., Mathiyarasu, J. & Kim, B. -S. Environmental-assisted simple synthesis and electrocatalytic performance of Ni-MOF nanorods. *Electrochim. Acta*. **462**, 142798 (2023).
17. Lee, M. G., Radhakrishnan, S., Ko, T. H. & Kim, B. S. Facile fabrication of flower—like Ni-Co-Mn-based LDHs and their superior catalytic performance for atenolol, nitrite and methanol. *J. Environ. Chem. Eng.* **10**, 108721 (2022).
18. Yang, Z., Liu, T., Wang, W. & Zhang, L. Stacked hexagonal prism of Ag@Ni-MOF-1 as functionalized SERS platform through rational integration of catalytic synthesis of dopamine-quinone at physiological pH with a biomimetic route. *Chem. Commun. (Camb.)*. **56**, 3065–3068 (2020).
19. Kavya, K. V. et al. Palladium nanoparticles decorated Ni-MOF nanocomposite as an electrochemical platform for the selective detection of dopamine. *Mater. Lett.* **306**, 130926 (2022).
20. Ibrahim, I., Lim, H. N., Huang, N. M., Jiang, Z. T. & Altarawneh, M. Selective and sensitive visible-light-prompt photoelectrochemical sensor of Cu^{2+} based on CdS nanorods modified with au and graphene quantum dots. *J. Hazard. Mater.* **391**, 122248 (2020).
21. Lima, D., Calaça, G. N., Viana, A. G. & Pessôa, C. A. Porphyran-Capped gold nanoparticles modified carbon paste electrode: a simple and efficient electrochemical sensor for the sensitive determination of 5-fluorouracil. *Appl. Surf. Sci.* **427**, 742–753 (2018).
22. Wang, C. et al. Facile preparation and catalytic performance characterization of AuNPs-loaded hierarchical electrospun composite fibers by solvent vapor annealing treatment. *Colloids Surf. A*. **561**, 283–291 (2019).
23. Lu, S. et al. Synthesis of Au@ZIF-8 nanocomposites for enhanced electrochemical detection of dopamine. *Electrochem. Commun.* **114**, 106715 (2020).
24. van Mourik, T., Buhl, M. & Gaigeot, M. P. Density functional theory across chemistry, physics and biology. *Philos. Trans. Math. Phys. Eng. Sci.* **372**, 20120488 (2014).
25. Sivaprakasam Radhakrishnan, S. C. S., Noh, J. H. & Ko, T. H. Byoung-Suhk Kim A portable highly uniform and reproducible microflower CuS/rGO hybrid sensor: an effective electrochemical and DFT evaluation method for Nitrite in water. *J. Environ. Chem. Eng.* **11**, 110057 (2023).
26. Ortiz-Medina, J. et al. Differential Response of Doped/Defective graphene and dopamine to Electric fields: a density functional theory study. *J. Phys. Chem. C.* **119**, 13972–13978 (2015).
27. Du, P. et al. Fabrication of hierarchical porous nickel-based metal-organic framework (Ni-MOF) constructed with nanosheets as novel pseudo-capacitive material for asymmetric supercapacitor. *J. Colloid Interface Sci.* **518**, 57–68 (2018).
28. Bodkhe, G. A. et al. Selective and sensitive detection of lead pb(II) ions: Au/SWNT nanocomposite-embedded MOF-199. *J. Mater. Sci.* **56**, 474–487 (2020).
29. Thommes, M. et al. Physisorption of gases, with special reference to the evaluation of surface area and pore size distribution (IUPAC Technical Report). *Pure Appl. Chem.* **87**, 1051–1069 (2015).

30. Lv, L. et al. A signal off aptasensor based on AuNPs/Ni-MOF substrate-free catalyzed for detection Enrofloxacin. *J. Electroanal. Chem.* **911**, 116251 (2022).
31. Meng, C. et al. A Ni-MOF nanosheet array for efficient oxygen evolution electrocatalysis in alkaline media. *Inorg. Chem. Front.* **8** (12), 3007–3011 (2021).
32. Stoll, S. et al. Photodegradation of MC-LR using a novel Au-decorated Ni metal-organic framework (Au/Ni-MOF). *Chemosphere* **344**, 140404 (2023).
33. Thambiraj, S. & Hema, S. & Ravi Shankaran, D. Functionalized gold nanoparticles for drug delivery applications. *Mater. Today Proc.* **5**, 16763–16773 (2018).
34. Qiao, Y. et al. High-performance non-enzymatic glucose detection: using a conductive Ni-MOF as an electrocatalyst. *J. Mater. Chem. B.* **8**, 5411–5415 (2020).
35. Gong, C., Li, Z., Liu, G., Wang, R. & Pu, S. A sensitive fluorescence turn on nanosensor for glutathione detection based on Ce-MOF and gold nanoparticles. *Spectrochim. Acta Mol. Biomol. Spectrosc.* **265**, 120362 (2022).
36. Young, A. J. et al. One-step synthesis and XPS investigations of chiral NHC-Au(0)/Au(i) nanoparticles. *Nanoscale* **11**, 8327–8333 (2019).
37. Zhang, Y., Hu, Y., Li, G. & Zhang, R. A composite prepared from gold nanoparticles and a metal organic framework (type MOF-74) for determination of 4-nitrothiophenol by surface-enhanced Raman spectroscopy. *Mikrochim. Acta.* **186**, 477 (2019).
38. Fan, T. et al. Synthesis of hierarchical porous ZIF-8/3DCNTs composite sensor for ultrasensitive detection of DA and DFT studies. *J. Electroanal. Chem.* **878**, 114541 (2020).
39. Xiao, L., Zheng, S., Yang, K., Duan, J. & Jiang, J. The construction of CoP nanoparticles coated with carbon layers derived from core-shell bimetallic MOF for electrochemical detection of dopamine. *Microchem. J.* **168**, 106432 (2021).
40. Lestari, W. W. & a., I. D. W. 2. Electrosynthesis of metal-organic frameworks (MOFs)based on Nickel(II) and Benzene 1,3,5-tri carboxylic acid (H3BTC): an optimization reaction condition. *Mater. Sci. Eng. B.* **172**, 012064 (2017).
41. Wei, F., Chen, D., Liang, Z., Zhao, S. & Luo, Y. Synthesis and characterization of metal-organic frameworks fabricated by microwave-assisted ball milling for adsorptive removal of Congo red from aqueous solutions. *RSC Adv.* **7**, 46520–46528 (2017).
42. Lv, Y. & Hao, X. R. Crystal structure of a binuclear nickel(II) complex constructed of 1H-imidazo[4,5-f][1,10]phenanthroline and doubly deprotonated benzene-1,3,5-tri-carb-oxy-lic acid. *Acta Crystallogr. E Crystallogr. Commun.* **71**, m95–96 (2015).
43. Jiang, H., Wang, Q., Wang, H., Chen, Y. & Zhang, M. MOF-74 as an efficient catalyst for the low-temperature selective catalytic reduction of NO_x with NH_3. *ACS Appl. Mater. Interfaces.* **8**, 26817–26826 (2016).
44. Luo, Y. C. et al. Heterogenization of photochemical molecular devices: embedding a metal-organic cage into a ZIF-8-derived matrix to promote proton and electron transfer. *J. Am. Chem. Soc.* **141**, 13057–13065 (2019).
45. Duan, C. & Zheng, J. Bimetallic MOF-based enzyme-free sensor for highly sensitive and selective detection of dopamine. *J. Electrochem. Soc.* **166**, B942–B947 (2019).
46. Li, G., Liu, S., Liu, D. & Zhang, N. MOF-derived porous nanostructured Ni_2P/C material with highly sensitive electrochemical sensor for uric acid. *Inorg. Chem. Commun.* **130**, 108713 (2021).
47. Wang, X. L. et al. Synthesis, structures and electrochemical properties of two novel metal-organic coordination complexes based on trimesic acid (H_3BTC) and 2,5-bis(3-pyridyl)-1,3,4-oxadiazole (BPO). *Solid State Sci.* **11**, 2118–2124 (2009).
48. Wu, K. Y. et al. Facile and recyclable dopamine sensing by a label-free terbium(III) metal-organic framework. *Talanta* **221**, 121399 (2021).
49. Xie, F. et al. MOF-cloth formed via supramolecular assembly of NH_2-MIL-101(cr) crystals on dopamine modified polyimide fiber for high temperature fume paper-based filter. *Compos. Part. B Eng.* **168**, 406–412 (2019).
50. Liu, K., Chen, Y., Dong, X. & Huang, H. Simultaneous voltammetric determination of dopamine and uric acid based on MOF-235 nanocomposite. *Inorg. Chem. Commun.* **142**, 109584 (2022).
51. Yao, W. et al. Highly electrochemical performance of Ni-ZIF-8/N S-CNTs/CS composite for simultaneous determination of dopamine, uric acid and L-tryptophan. *Microchem. J.* **152**, 104357 (2020).
52. Zhou, F. et al. Simultaneous electrochemical detection of dopamine and uric acid via Au@Cu-metal organic framework. *Chempluschem* e202300686 (2024).
53. Zhao, D., Yu, G., Tian, K. & Xu, C. A highly sensitive and stable electrochemical sensor for simultaneous detection towards ascorbic acid, dopamine, and uric acid based on the hierarchical nanoporous PtTi alloy. *Biosens. Bioelectron.* **82**, 119–126 (2016).
54. Lin, K. C., Tsai, T. H. & Chen, S. M. Performing enzyme-free H_2O_2 biosensor and simultaneous determination for AA, DA, and UA by MWCNT-PEDOT film. *Biosens. Bioelectron.* **26**, 608–614 (2010).
55. Silva, L. V. et al. Amperometric sensor based on carbon nanotubes and electropolymerized vanillic acid for simultaneous determination of ascorbic acid, dopamine, and uric acid. *J. Solid State Electrochem.* **20**, 2389–2393 (2016).
56. Dos Santos, P. L., Katic, V., Toledo, K. C. F. & Bonacin, J. A. Photochemical one-pot synthesis of reduced graphene oxide/Prussian blue nanocomposite for simultaneous electrochemical detection of ascorbic acid, dopamine, and uric acid. *Sens. Actuators B Chem.* **255**, 2437–2447 (2018).
57. Rad, A. S., Shahavi, M. H., Esfahani, M. R., Darvishinia, N. & Ahmadizadeh, S. Are nickel- and titanium-doped fullerenes suitable adsorbents for dopamine in an aqueous solution? Detailed DFT and AIM studies. *J. Mol. Liq.* **322**, 114942 (2021).
58. Keypour, H. et al. Synthesis and characterization of Co(II), ni(II), Cu(II) and zn(II) complexes with a new homopiperazine macrocyclic Schiff base ligand. *Inorg. Chim. Acta.* **432**, 243–249 (2015).
59. Silvarajoo, S. et al. Dataset of theoretical molecular electrostatic potential (MEP), highest occupied molecular orbital-lowest unoccupied molecular orbital (HOMO-LUMO) band gap and experimental cole-cole plot of 4-(ortho-, meta- and para-fluorophenyl)thiosemicarbazide isomers. *Data Brief.* **32**, 106299 (2020).
60. Osman, U. M. et al. Correlation data of (Z)-1-[4-(trifluoromethyl) benzylidene] thiosemicarbazide via spectroscopic methods and density functional theory studies. *Data Brief.* **27**, 104673 (2019).

Acknowledgements

This work was financially supported by the Tianchi Doctor Program of Xinjiang Uygur Autonomous Region (Grant No.: 2024000071) and Special Innovation Projects for Ordinary Universities in Guangdong Province (no. 2022KTSCX167). The authors appreciate Prof. Dr. Hui Yin from Xinjiang Institute of Ecology and Geography Chinese Academy of Sciences for her support in the SEM and EDX measurements.

Author contributions

F.Z. wrote the main manuscript text and prepared all the figures. All authors reviewed the manuscript.

Declarations

Competing interests

The authors declare no competing interests.

Additional information

Supplementary Information The online version contains supplementary material available at https://doi.org/10.1038/s41598-025-89797-1.

Correspondence and requests for materials should be addressed to L.G. or Y.L.

Reprints and permissions information is available at www.nature.com/reprints.

Publisher's note Springer Nature remains neutral with regard to jurisdictional claims in published maps and institutional affiliations.

Open Access This article is licensed under a Creative Commons Attribution-NonCommercial-NoDerivatives 4.0 International License, which permits any non-commercial use, sharing, distribution and reproduction in any medium or format, as long as you give appropriate credit to the original author(s) and the source, provide a link to the Creative Commons licence, and indicate if you modified the licensed material. You do not have permission under this licence to share adapted material derived from this article or parts of it. The images or other third party material in this article are included in the article's Creative Commons licence, unless indicated otherwise in a credit line to the material. If material is not included in the article's Creative Commons licence and your intended use is not permitted by statutory regulation or exceeds the permitted use, you will need to obtain permission directly from the copyright holder. To view a copy of this licence, visit http://creativecommons.org/licenses/by-nc-nd/4.0/.

© The Author(s) 2025